JOURNAL OF SPACECRAFT AND ROCKETS
Vol. 42, No. 2, March–April 2005

# Self-Pressurization of Large Spherical Cryogenic Tanks in Space

Charles H. Panzarella*
*Ohio Aerospace Institute, Cleveland, Ohio 44142*
and
Mohammad Kassemi†
*NASA John H. Glenn Research Center at Lewis Field, Cleveland, Ohio 44135*

**The pressurization of large cryogenic storage tanks under microgravity conditions is investigated by coupling a lumped thermodynamic model of the vapor region with a complete solution of the flow and temperature fields in the liquid. Numerical results indicate that in microgravity both buoyancy and natural convection are still important and play a significant role in phase distribution and tank pressurization. A spherical vapor region initially placed at the center of the tank deforms and moves to one side of the tank before any significant pressure rise. Long-term results obtained with the vapor region near the tank wall show that, even in microgravity, natural convection leads to thermal stratification in the liquid and significantly alters the initial pressure rise. The final rate of pressure rise agrees with a lumped thermodynamic model of the entire system, but the final pressure levels depart from thermodynamic predictions because of initial transients. The history of the maximum liquid superheat and subcooling is also determined for each configuration.**

## Nomenclature

$c$ = specific heat, erg/K · g
$g$ = gravitational acceleration, cm/s$^2$
$k$ = thermal conductivity, erg/cm · s · K
$L$ = latent heat of vaporization, erg/g
$m$ = molar mass, g/mol
$p$ = pressure, Pa
$Q$ = net heat flow, W
$q$ = heat flux, W/cm$^2$
$R$ = spherical tank radius, cm
$R_g$ = ideal gas constant, erg/K · mol
$r, z$ = cylindrical coordinates, cm
$T$ = temperature, K
$t$ = time, s
$V$ = volume, cm$^3$
$\beta$ = thermal expansion coefficient, 1/K
$\mu$ = dynamic viscosity, g/cm · s
$\rho$ = density, g/cm$^3$

*Subscripts*

$b$ = normal boiling point
$l$ = liquid phase
max = maximum
$s$ = saturation
$v$ = vapor phase
$w$ = tank wall

## Introduction

THE extension of human space exploration from low Earth orbit into the solar system is one of NASA's biggest challenges for the next millennium. The projected exploration programs include a series of human and robotic expeditions to low and high Earth orbit, the moon, Mars, and possibly to the asteroids and other planetary moons. Integral to all phases of these space and planetary expeditions is effective, affordable, and reliable cryogenic fluid management for use in the propellant and life-support systems. Without safe and efficient cryogen storage, economically feasible and justified human missions will not be possible.

With the exception of extremely short-duration missions, significant cost savings can be achieved if the launch mass can be reduced by improving the cryogenic storage and transfer technologies.[1] Cryogen vaporization is one of the main causes of mass loss and leads to the self-pressurization of the storage tanks.[2] Vaporization can occur during the filling process, or may be caused by heat leaks into the tank from the surrounding environment. Ordinarily, the excess pressure can be relieved by direct venting to the environment. For on-surface applications, such as those on the surface of the Earth, moon, or Mars, the spatial configuration of liquid and vapor is dictated by gravity and is well known. In this situation, continuous venting can be easily accomplished; but over a significant length of time it results in considerable cryogen mass loss. For in-space applications, the spatial configuration of liquid and vapor is generally unknown, and direct venting without prepositioning of the two phases is precluded due to the possibility of expelling liquid along with the vapor. Moreover, venting in space is also undesirable because it prohibits manned flight operations around the storage tanks.

Therefore, from both safety and cryogen conservation viewpoints, a ventless pressure control strategy is highly desirable for both on-surface and in-space applications. The zero boil-off (ZBO) pressure control strategy has been proposed as an effective means of achievement of ventless storage through the synergetic application of active cooling and mixing. The cooling can be achieved by the use of cryocoolers, and the mixing is normally provided by impellers or forced liquid jets. The transport mechanisms in such a situation can be extremely complex and require hand-in-hand experimental and theoretical elucidation before they are applied in practice.

The self-pressurization of cryogen storage tanks has been the subject of many previous experimental investigations. (See Ref. 3 for a somewhat comprehensive list.) However, very few have considered the differences due to reduced-gravity conditions. One such work[4] shows that the initial rate of pressurization is lower under reduced-gravity conditions than under normal-gravity conditions, and this was primarily attributed to an increase in the tank wall surface area covered by liquid. Other aspects of cryogen storage have been considered, such as the effect of a liquid jet on the bulk mixing behavior[5,6] and its ability to control the tank pressure[7] and reduce thermal stratification.[8]

---

Received 25 November 2003; revision received 13 March 2004; accepted for publication 16 March 2004.

*Senior Scientist, 22800 Cedar Point Road; Charles.H.Panzarella@grc.nasa.gov. Member AIAA.

†Deputy Chief Scientist, National Center for Microgravity Research, 21000 Brookpark Road, Mailstop 105-1. Member AIAA.

Previous numerical studies of tank pressurization have been primarily limited to purely thermodynamic treatments,[9–11] fluid flow, and thermal stratification in the liquid without any consideration of the resultant pressure rise in the vapor,[12–17] or the evolution of the phase distribution without any thermal considerations.[18–25]

Panzarella and Kassemi[3] have developed a more comprehensive numerical model by coupling a lumped thermodynamic treatment of the vapor region with a direct numerical simulation of the Navier–Stokes, energy, and continuity equations in the liquid region. In this way, the effect of the heat and mass transport in the liquid region on the tank pressure rise can be determined. This approach has already been used to investigate the pressurization of a small ground-based tank,[3] where it was shown that the initial rate of pressurization depends on the particular heat flux distribution prescribed on the tank wall, even though the long-term rate of pressurization agrees with a purely thermodynamic description of the entire tank. It was also shown that the pressure rise in a ground-based tank could be controlled by the use of a subcooled liquid jet.

The present work uses the same approach to investigate the pressure rise for a large tank in microgravity. In microgravity, the vapor region could be anywhere in the tank, but the first set of results will show that buoyancy forces bring it right next to the tank wall in a short amount of time compared to the conduction and convection timescales. Consequently, long-term pressurization is examined with the vapor region fixed near the tank wall. The results will also show significant differences between the zero-gravity and microgravity environments even though the final rate of pressurization agrees with thermodynamics. For each configuration considered here, the time evolution and spatial distribution of the liquid superheat and subcooling are also determined.

## Cryogenic Tank Model

This paper considers a large spherical tank in microgravity filled with liquid hydrogen and its saturated vapor as illustrated in Fig. 1. This is similar to the model developed previously to study ground-based pressurization,[3] except for the initial configuration of liquid and vapor. It is assumed that the vapor region is initially spherical, located at the center of the tank, and completely surrounded by liquid. A cylindrical coordinate system is used with the origin at the center of the tank and with the $z$ axis antiparallel to the direction of gravity. A typical average acceleration for microgravity is assumed to be $g = 981 \times 10^{-6}$ cm/s$^2$. Comparisons are also made to solutions obtained in zero gravity. The problem is assumed to be axisymmetric with respect to the $z$ axis. The tank is heated by prescription of the steady heat flux $q_w$ uniformly across the entire tank wall surface.

The liquid is treated as an incompressible, Newtonian fluid with constant properties as described by the standard time-dependent Navier–Stokes, energy, and continuity equations. The Boussinesq approximation is used to account for buoyancy effects. The vapor is treated as an inviscid, compressible, ideal gas with spatially uniform temperature, pressure, and density. It is assumed to be in thermal equilibrium with the surrounding liquid as dictated by the Clausius–Clapeyron equation for an ideal gas (see Ref. 26).

The temperature at the liquid–vapor interface is set equal to the saturation temperature corresponding to the vapor pressure. The interface is treated as a free surface for the first set of short-duration results, but for longer-duration studies, it is forced to remain spherical. Even so, fluid is still allowed to flow over its surface by imposition of a zero tangential-stress boundary condition at the interface and by solution of the tangential velocity.

It is assumed that the liquid–vapor interface does not move due to evaporation, so that the liquid and vapor volumes remain constant during the simulation. The liquid volume would actually decrease over time as liquid evaporated, but for the values of $Q_l$ determined here, the total mass of evaporated liquid is never greater than about 1% of the initial liquid mass. Thus, for the present cases, this is not a bad assumption.

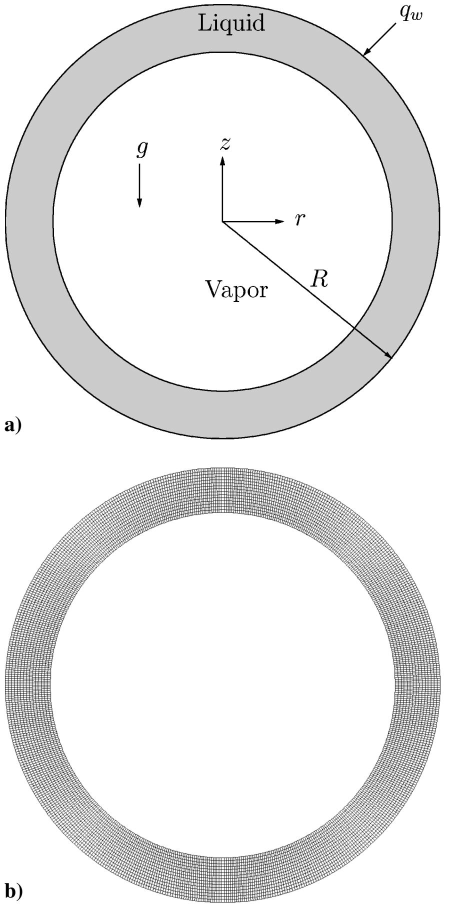

**Fig. 1 Space-based cryogenic tank model considered here assumes the vapor initially occupies a single spherical region completely surrounded by liquid; also shown is typical numerical mesh for 50% full tank consisting of 5178 nine-node elements (17,763 nodes).**

A lumped-vapor model determines the vapor pressure rise due to any net heat and mass transfer into the vapor region.[3] The final result is a single evolution equation for the vapor pressure,

$$\dot{p}_v = F(p_v)(Q_l + Q_v) \tag{1}$$

where $Q_l$ is the net heat entering the vapor region through the surrounding liquid, $Q_v$ is the net heat entering the vapor directly through the tank wall, and $F$ is given by

$$F(p_v) = (L/V_v)\{c_v T_s + (Lm/R_g T_s - 1)[\rho_l/(\rho_l - \rho_v)] \\ \times [L - p_v(1/\rho_v - 1/\rho_l)]\}^{-1} \tag{2}$$

$Q_v$ is zero if the vapor is completely surrounded by liquid, and $Q_l$ is obtained by integration of the liquid-side heat flux over the entire free surface.

Comparisons are also made to a lumped thermodynamic model of the entire tank as described by the following equations, which represent global energy, mass, and volume balances, respectively:

$$\frac{\mathrm{d}}{\mathrm{d}t}(\rho_l V_l c_l T + \rho_v V_v c_v T) + p\frac{\mathrm{d}}{\mathrm{d}t}(V_l + V_v) = Q_w \tag{3a}$$

$$\frac{\mathrm{d}}{\mathrm{d}t}(\rho_l V_l + \rho_v V_v) = 0 \tag{3b}$$

$$\frac{\mathrm{d}}{\mathrm{d}t}(V_l + V_v) = 0 \tag{3c}$$

These are solved along with the ideal gas law and the saturation temperature condition to obtain the pressure rise in the tank from purely thermodynamic considerations. The work term in Eq. (3a) is automatically zero during storage because the total volume remains constant.

The governing equations are solved by the use of an in-house modified version of the commercial finite element code FIDAP.[27] It is modified to include the coupled solution of the lumped-vapor analysis, along with the standard solution of the Navier–Stokes, energy, and continuity equations for the liquid region. Additional details about this approach and studies of the spatial and temporal convergence for a similar problem can be found in Ref. 3.

The liquid domain is partitioned into a number of nine-node quadratic interpolation elements. The number of elements in the mesh varies from between 1470 and 5178, depending on the case, and the mesh is refined in regions of steeper solution gradients. A typical mesh is shown in Fig. 1. The mesh deforms by the use of the method of spines as the vapor region moves. If the mesh becomes too distorted, then the solution is halted and then restarted with a more uniform mesh, and the old solution is interpolated onto the new mesh to obtain the updated initial conditions. At each time step, an iterative solution strategy is employed to solve the resulting matrix equations with a relative convergence tolerance of $10^{-6}$. Timesteps are chosen adaptively to keep an estimate of the time truncation error less than $10^{-5}$ (Ref. 28).

The approximate computation time for the following cases varied from between 10 CPU minutes for the zero-gravity cases to as long as three days for some of the microgravity cases with a moving vapor region. These results were obtained on a 1.6-GHz Intel Xeon computer system with 16 GB of memory running the Red Hat Linux 7.3 operating system.

## Results and Discussion

The results of the numerical simulations will be presented in terms of the time evolution of the vapor pressure, saturation temperature, maximum liquid superheat and subcooling, and the net interfacial heat flow into the vapor region. Representative streamline and temperature fields in the liquid region are also presented at given times. These fields are shown by 10 equally spaced temperature and/or streamline contours between the minimum and maximum values. To save space and because the solution is axisymmetric, these contour plots are combined into a single image with the isotherms on the left and the streamlines on the right. The material properties and other model parameters used here are listed in Table 1.

### Zero-Gravity Case Studies

For the zero-gravity results, the vapor region is assumed to be spherical and located either at the center of the tank or near the wall with an arbitrary spacing of 1 mm between the vapor and tank wall. The actual gap thickness does not matter that much because the heat flux across any sufficiently thin liquid film would be nearly the same as the prescribed tank-wall heat flux. The solution for any other position should lie somewhere between these two extremes. The liquid is initially motionless with a uniform temperature of 20 K, and the vapor is in equilibrium with the surrounding liquid.

The pressure rise for these two configurations is shown in Fig. 2 for liquid fill levels of 50 and 95%, and the corresponding saturation temperatures are shown in Fig. 3. It is clear that the pressure rises more rapidly at first when the vapor region is closer to the wall, but eventually the rate of pressure rise is the same in all cases and in agreement with the lumped thermodynamic model of the entire tank. With the vapor region centered, it takes a couple of days before such agreement is reached for the 50% full tank and about 20 days for the 95% full tank. This is because the conduction timescale based on the distance between the tank wall and the liquid–vapor interface, $(R - R_v)^2 \rho_l c_l / k_l$, is very long to begin with, but is even longer for larger fill levels. When the vapor is near the wall, agreement is achieved much more quickly, especially for the 95% fill level.

**Table 1 Material properties of hydrogen at the normal boiling point temperature (20.39 K) and other model parameters**

| Parameter | Value |
|---|---|
| $\beta_l$ | 0.0175 |
| $c_l$ | $9.7 \times 10^7$ |
| $c_v$ | $1.012 \times 10^8$ |
| $g$ | $981 \times 10^{-6}$ |
| $k_l$ | 12440 |
| $L$ | $4.456 \times 10^9$ |
| $m$ | 2.0 |
| $\mu_l$ | $1.327 \times 10^{-4}$ |
| $p_b$ | $1.014 \times 10^5$ |
| $q_w$ | $10^{-5}$ |
| $Q_w$ | 2.827 |
| $R$ | 150 |
| $R_g$ | $8.31 \times 10^7$ |
| $\rho_l$ | 0.07047 |
| $\rho_v$ | 0.00133 |
| $\sigma$ | 1.93 |
| $T_b$ | 20.39 |

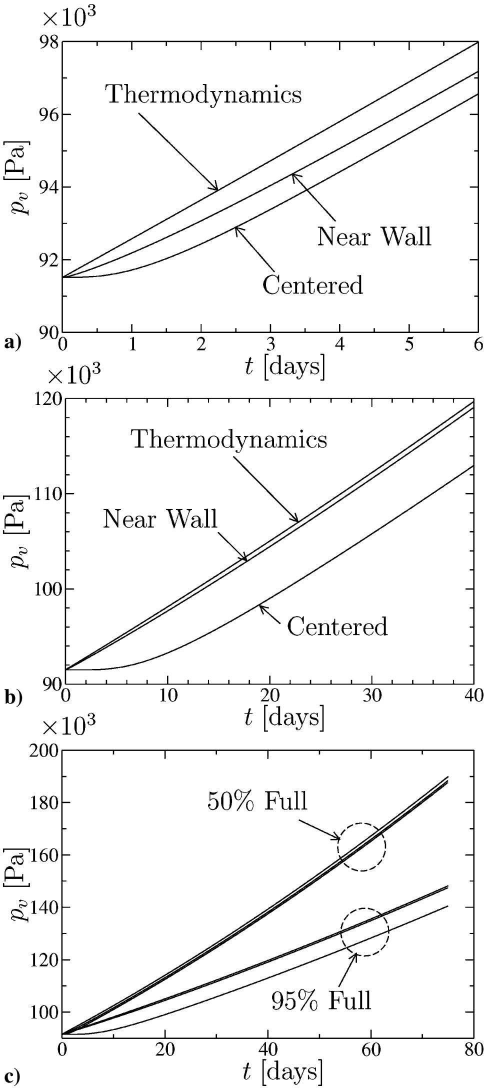

**Fig. 2 Pressure rise for a) 50%, b) 95% full tank in zero gravity with the spherical vapor region centered or fixed near the wall, and c) long-term results for both fill levels.**

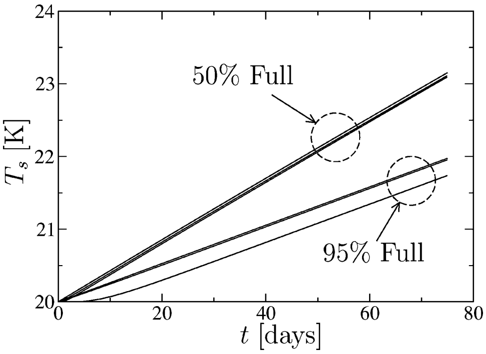

**Fig. 3 Long-term saturation temperatures corresponding to the vapor pressures shown in Fig. 2.**

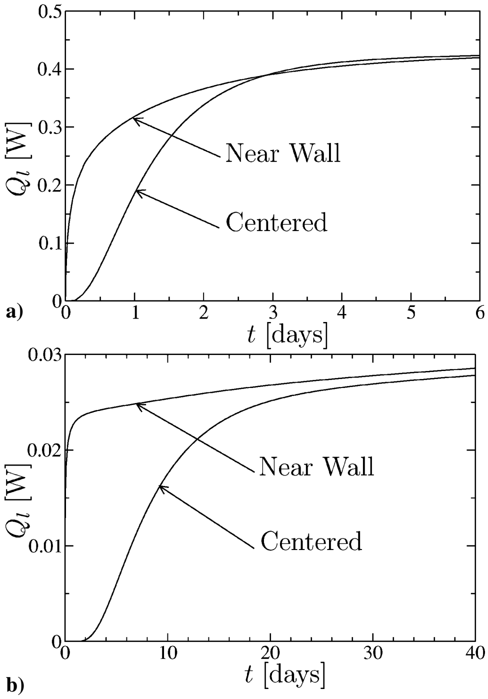

**Fig. 4 Net heat flow into the vapor region through the free surface for the a) 50% and b) 95% full tank in zero gravity.**

The net heat flow into the vapor region is shown in Fig. 4. When the vapor is close to the wall, $Q_l$ has a quick initial rise but becomes nearly constant later on as the temperature solution in the liquid approaches a stationary state in which the temperature gradients remain nearly the same even though the average temperature keeps on rising. This stationary state was observed in previous numerical simulations of smaller ground-based tanks,[3] where a perfectly stationary thermal gradient field was attained in the liquid region.

In the present situation, this stationary state is never perfectly achieved because the relative pressure changes are much greater. This follows from the increased surface area of the larger tank, which, for the same tank-wall heat flux, leads to a greater total heat input, and the nonlinear nature of the pressure–temperature saturation curve is no longer negligible over the period of time required to achieve the stationary state. This leads to a very slight upward bending of the pressure curves and a slight downward bending of the corresponding saturation temperature curves, whereas in the smaller, ground-based tank these curves were perfectly straight. Note also that the thermodynamic pressure curve is bending in the same manner, and so this is an effect that can be captured by the simpler model as well.

The temperature field corresponding to this stationary state after a period of 75 days is shown in Fig. 5 for the 50% full tank and in Fig. 6 for the 95% full tank. Because the interfacial temperature is set equal to the saturation temperature, any deviation from that temperature represents a local superheat or subcooling of the liquid at that point. Thus, the isotherms shown here actually represent the distribution of the superheat and subcooling throughout the liquid. Knowing the distribution of the superheat is important because the onset of nucleate boiling is most likely to occur in regions of maximum superheat, and this could lead to undesirable pressure spikes as stored thermal energy is suddenly released by boiling. This model is able to predict the location and magnitude of the maximum superheat for different liquid–vapor configurations, and this information could be used to compute the probability of vapor bubble nucleation.

For the 50% full tank shown in Fig. 5a, the final maximum superheat is 0.166 K at the wall, and the subcooling is zero because the bubble is centered. With the vapor region near the wall as in Fig. 5b, the final maximum superheat is slightly larger at 0.170 K, and there is also a maximum subcooling of 0.0497 K in the midst of the liquid beneath the vapor region. The history of the maximum superheat and subcooling is shown in Figs. 7 and 8, along with the values for all of the other cases examined here. The superheat and subcooling both approach constant values in each case as the temperature field approaches the stationary state.

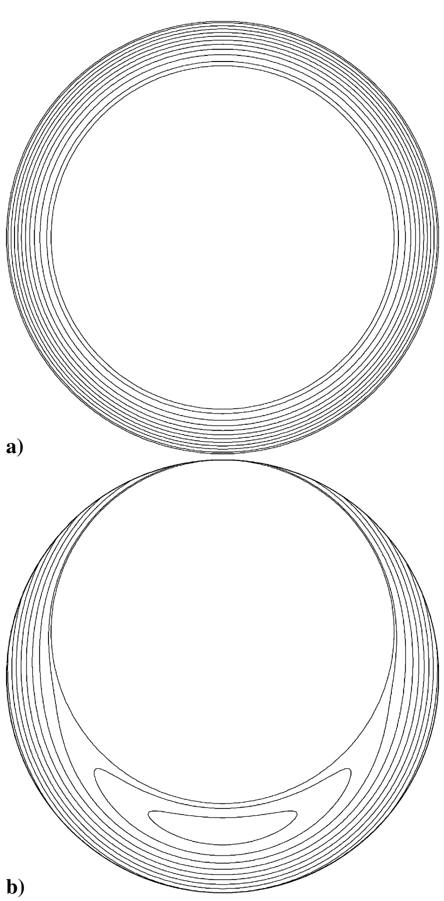

**Fig. 5 Final isotherms at $t = 75$ days for a 50% full tank in zero gravity with a spherical vapor region that is a) centered or b) near the wall; minimum and maximum temperatures are a) 23.092 and 23.2577 K and b) 23.061 and 23.281 K.**

The subcooling arises because the liquid region requires a larger fraction of the total heat input to maintain the same rate of average temperature rise as the vapor. Because the vapor is so close to the wall, it receives more heat than it actually needs, and this excess heat is released into the underlying liquid giving rise to the observed subcooling.

For the 95% full tank shown in Fig. 6a, the final maximum superheat is 0.457 K at the wall, and the subcooling is zero because the vapor is centered. The maximum superheat is larger than for the 50% full tank because the vapor is further away from the wall. When the vapor region is closer to the wall as in Fig. 6b, the final maximum superheat decreases to 0.271 K, and a maximum subcooling of 0.305 K arises near the center of the tank as excess heat received by the vapor is released into the underlying liquid. The maximum superheat still occurs on the tank wall, but not at the point where the vapor is closest to the wall as one might think. This is because the temperature drop across the intervening liquid film must approach zero as its thickness approaches zero to satisfy the constant heat flux boundary condition prescribed on the tank wall. The history of the maximum superheat and subcooling for this case is also shown in Figs. 7 and 8.

### Microgravity Case Studies

The microgravity investigations are further divided into two cases. In the first case, the spherical vapor region is initially centered, and the history of the tank pressure, as well as the evolution of the liquid flow and thermal fields, are examined by following the deforming vapor region as it approaches the tank wall. The initial conditions

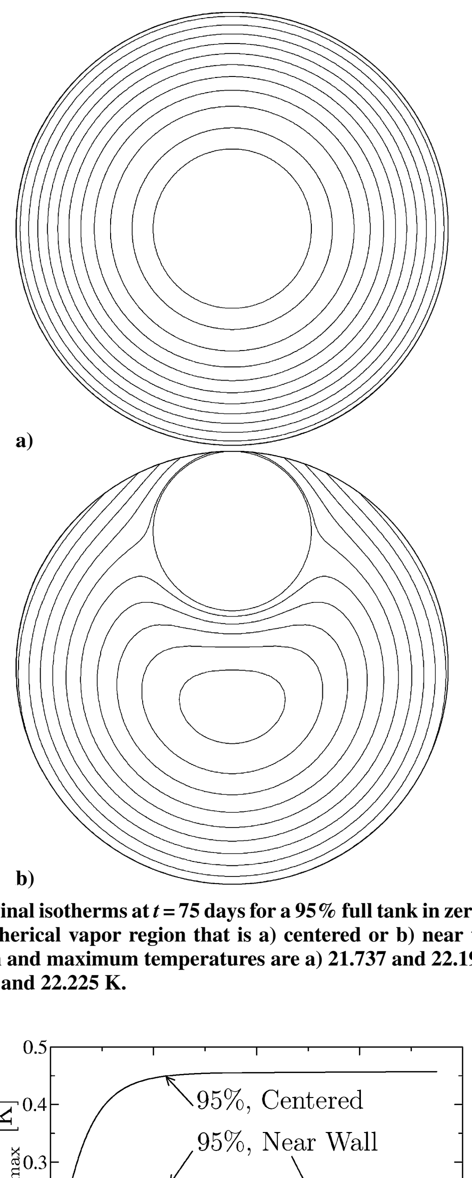

**Fig. 6 Final isotherms at $t = 75$ days for a 95% full tank in zero gravity with a spherical vapor region that is a) centered or b) near the wall; minimum and maximum temperatures are a) 21.737 and 22.194 K and b) 21.649 and 22.225 K.**

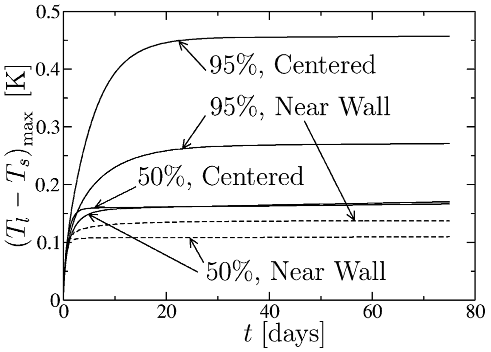

**Fig. 7 History of the maximum superheat for both the 50 and 95% full tank in ——, zero gravity and – – –, microgravity.**

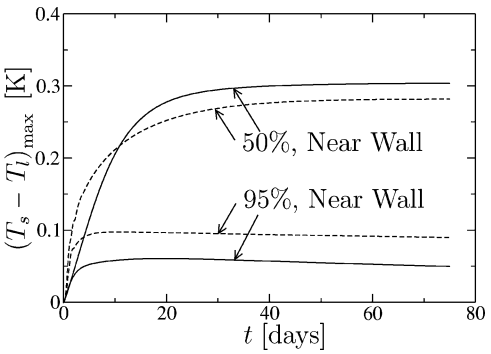

**Fig. 8 History of the maximum subcooling for both the 50 and 95% full tank in ——, zero gravity and – – –, microgravity.**

for the temperature and velocity are the same as before. It is shown that the vapor region reaches the wall after a short period of time relative to the conduction or convection timescales.

The second case study focuses on the temperature, pressure, and flowfields that develop over a longer time span, whereas the spherical vapor region is fixed near the wall. The free surface oscillations of the bubble are not accounted for, but fluid slip is allowed by the assumption that there is no shear stress on the vapor side of the interface. This permits us to study the average long-term pressurization without being limited by the smaller timesteps required to resolve the minor fluctuations caused by the surface oscillations.

Also note that the magnitude and direction of the acceleration vector are assumed to be constant here, whereas in reality they would undoubtedly fluctuate over time. However, as long as these fluctuations happen on a timescale much shorter than the other relevant timescales, the replacement of the actual acceleration profile with its time-averaged value is an acceptable approximation.

### *Moving Vapor Region*

The initially centered vapor region drifts upward due to buoyancy, as shown in Fig. 9a. For the 50% full tank, it takes less than 13 min for the vapor to reach the tank wall, which is not that surprising when one considers that, during that amount of time, the tank itself has moved a distance of about $gt^2/2 = 298$ cm, almost the entire tank diameter. The liquid is being dragged along by the tank wall, but this is countered by the liquid's own inertia, which will tend toward keeping it at the bottom of the tank.

The top of the vapor region flattens as it rises, and this brings the vapor nearest the tank wall not to the top as one might expect, but to a point further to the side. The liquid above this point is trapped momentarily and slowly drains downwards along the wall through a thin liquid film with a maximum speed of 1.27 cm/s in Fig. 9a and 1.24 cm/s in Fig. 9b. During this time, the thermal boundary layer

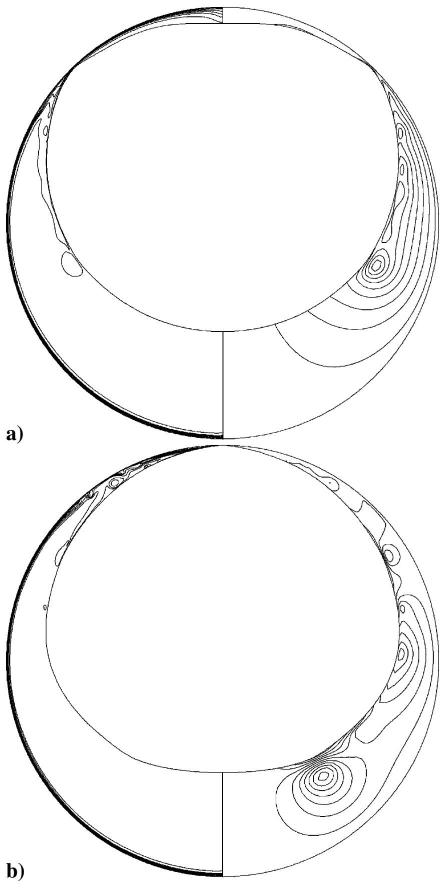

**Fig. 9 Isotherms and streamlines at a) $t = 791$ s and b) $t = 1014$ s for a 50% full tank in microgravity with an initially centered spherical vapor region.**

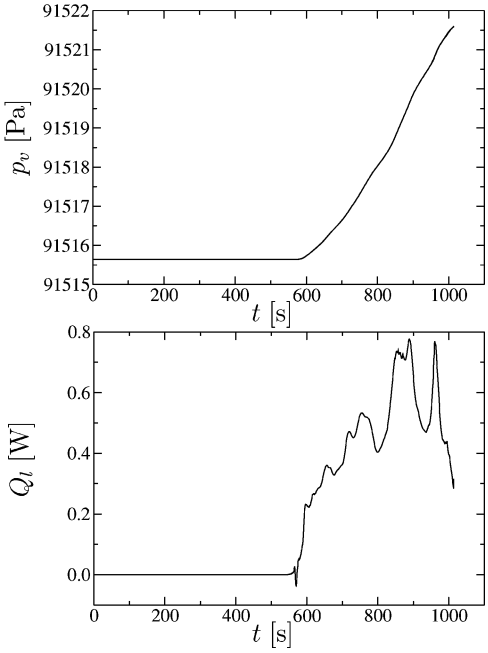

**Fig. 10 Pressure rise and net heat input for the case shown in Fig. 9.**

is still concentrated very close to the tank wall because the heat conduction timescale is measured in days for such a large tank, but, as a result of this drainage, a layer of warmer fluid near the wall is convected along the free surface and breaks up into a train of vortices as shown from the streamline plots in Fig. 9. After about 15 min, the liquid film has nearly finished draining, and the simulation is terminated because the distance between the interface and the tank wall becomes so small that it can no longer be justifiably resolved with the present free-surface methodology. It seems likely that the film would rupture past this point, leading to the formation of a vapor dry patch, but this cannot presently be determined.

The corresponding pressure rise and net heat flow for this case are shown in Fig. 10. Clearly, there is no heat flow into the vapor region, and, consequently, no pressure rise until the vapor gets very close to the wall. Then, the heat flow becomes very erratic because of the train of vortices and also because of the free-surface oscillations.

The maximum superheat and subcooling are, respectively, 0.0114 and 0.000422 K in Fig. 9a and 0.0123 and 0.000267 K in Fig. 9b. These are very small because the thermal boundary layer has not yet had enough time to develop sufficiently. The history of the maximum superheat and subcooling is also shown in Figs. 7 and 8.

A similar solution is obtained for the 95% full tank, as shown in Figs. 11 and 12. After only a few minutes, the vapor region is well on its way toward the wall as shown in Fig. 11a. At the intermediate time shown in Fig. 11b, the vapor region is clearly being pushed up against the wall with only a very thin liquid film in between. Eventually, surface tension pulls the vapor region back into a nearly spherical shape as shown in Fig. 11c, at which point the simulation is again terminated because the liquid film becomes too thin to be meaningfully resolved.

A well-known result from elementary fluid mechanics is that a vapor bubble initially at rest and surrounded by liquid will rise with an initial acceleration of $2g$ as long as $\rho_v \ll \rho_l$ (Ref. 29). This result comes from balancing the buoyancy force with the force required to accelerate the surrounding liquid (the added mass). Because the initial distance between the vapor and tank wall is 150 cm − 55.26 cm = 94.74 cm, a simple calculation based on this distance and acceleration would yield a time to reach the wall of 311 s. This is close to, but slightly less than, the time predicted by the model, but this is understandable due to the interference caused by the tank wall. This prediction is not as accurate for the 50% full tank because the vapor region quickly deforms from its spherical shape, and then it becomes a problem dictated by the draining liquid film, not buoyancy.

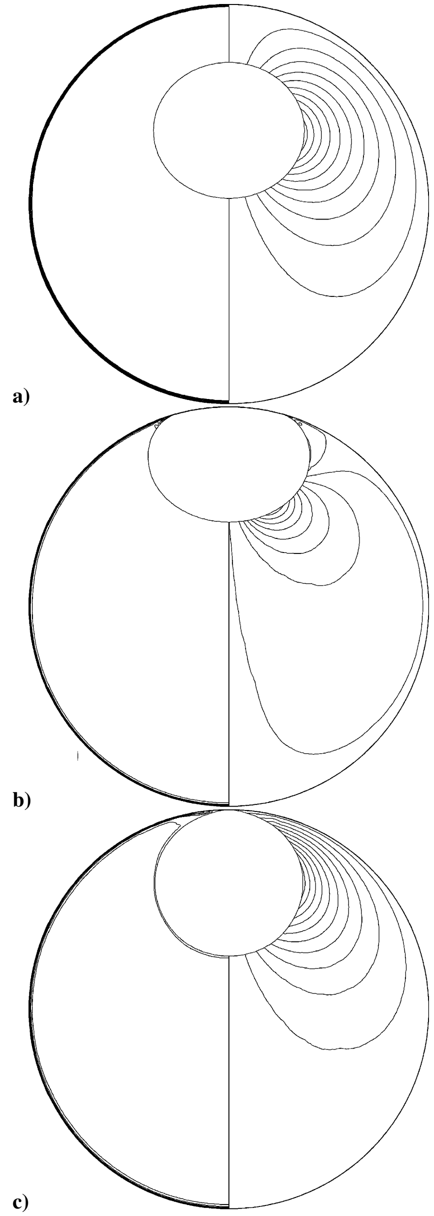

**Fig. 11 Isotherms and streamlines at a) $t = 259$ s, b) $t = 463$ s, and c) $t = 567$ s for a 95% full tank in microgravity with an initially centered spherical vapor region.**

While the vapor region is being pushed up against the wall, it receives an extra amount of heat as evidenced by the sharp upward spike in $Q_l$, as indicated in Fig. 12. However, once it begins to retract from the wall as surface tension forces try to restore its spherical shape, it no longer receives as much heat, and $Q_l$ decreases. Near the end of the simulation, the vapor has moved so far away from the wall that it receives hardly any additional heat, and, in fact, $Q_l$ becomes slightly negative as the excess heat stored in the vapor region gets released into the subcooled bulk liquid below.

The final maximum superheat and subcooling are, respectively, 0.00462 and 0 K in Fig. 11a, 0.00698 and 0.000168 K in Fig. 11b, and 0.00802 and 0.00147 K in Fig. 11c. Again, these values are extremely small because the thermal boundary layer has not yet fully developed. The history of the maximum superheat and subcooling is also shown in Figs. 7 and 8.

### *Stationary Vapor Region Near the Wall*

The preceding case study implied that after a relatively short period of time in microgravity, the vapor region will migrate close to the tank wall, provided that there is no major change in the average direction of the residual acceleration vector during that time. This

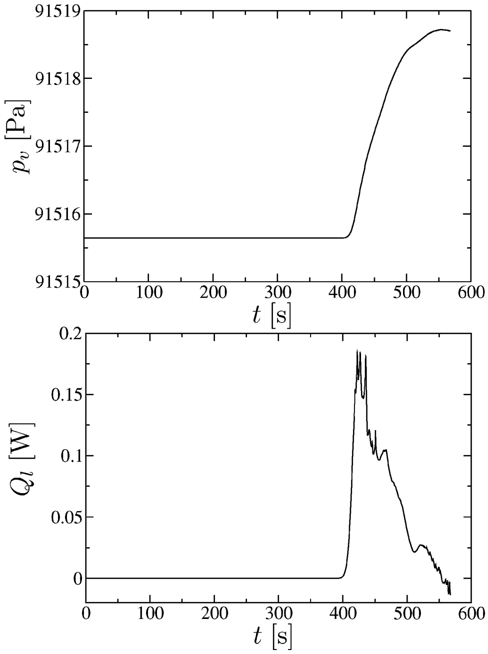

**Fig. 12 Pressure rise and net heat input for the case shown in Fig. 11.**

may eventually lead to the formation of dry patches if the vapor touches the wall, but the complex behavior of these dry patches is beyond the scope of the present paper.

Instead, we consider the following two limiting configurations. In the first, the vapor region is spherical and close to the tank wall. In the second, there is a flat interface separating liquid and vapor like the ground-based configuration. The actual configuration will lie somewhere between these two extremes. The importance of the flat-interface configuration is that it represents the limiting case where the maximum amount of vapor touches the tank wall in a stably stratified configuration. The real interface will likely never be completely flat, especially because the contact angle of liquid hydrogen is nearly zero. It is more likely that it would resemble an oblate spheroid in partial contact with the tank wall. The solution for that case would be very complex due to the motion of the dynamic contact line and cannot be considered with the present free-surface methodology. However, the pressure rise for that case would likely be bounded by the two limiting configurations considered here.

In the first case, the spherical vapor region is positioned near the wall such that the intervening liquid film is only 1-mm thick as shown for both fill levels in Fig. 13. As before, it is not allowed to move from this position or deform from its spherical shape, but liquid is allowed to slip over its surface.

By comparison of the resulting pressure, temperature, and heat input curves in Figs. 14–16 with those obtained previously under zero-gravity conditions, it is clear that, even in microgravity, natural convection still plays a significant role. Initially, the pressure rise agrees with the corresponding zero-gravity case, but, after 12 h, the additional heat carried by natural convection reaches the interface and causes the pressure to increase even faster and eventually surpass that predicted by thermodynamics.

There is a sudden increase in $Q_l$ as the warm fluid brought by natural convection reaches the interface as shown for both fill levels in Fig. 16, but, eventually, they both settle back down to the same constant value as before. The $Q_l$ curve for the 95% full tank shown in Fig. 16b exhibits more fluctuations early on due to a competition that arises between two counter-rotating convection cells in the tank. One of them brings warmer fluid near the wall up to the interface, whereas the other one brings cooler fluid from the bulk liquid, and this interplay manifests itself as the fluctuations in $Q_l$.

The final isotherms for both fill levels are shown in Fig. 13. These are noticeably different from the corresponding isotherms for the zero-gravity cases shown in Figs. 5 and 6 because they show significant thermal stratification due to natural convection. It might seem surprising to have thermal stratification in microgravity, but this can be understood when it is considered that the intensity of natural convection, as measured by the Grashof number $Gr = g\beta_l\rho_l^2 q_w R^4/k_l\mu_l^2$, is a very rapidly increasing function of the tank radius, whereas it is only linearly proportional to the gravitational acceleration. Thus, for the large tank in microgravity considered here, $Gr = 1.97 \times 10^7$, and this is very close to the value $Gr = 2.4 \times 10^7$ for the smaller 10-cm-diam ground-based cryogenic tank considered previously,[3] for which there was significant thermal stratification. For both cases, the Prandtl number is the same. Thus, it is not surprising that a similar degree of thermal stratification is observed here.

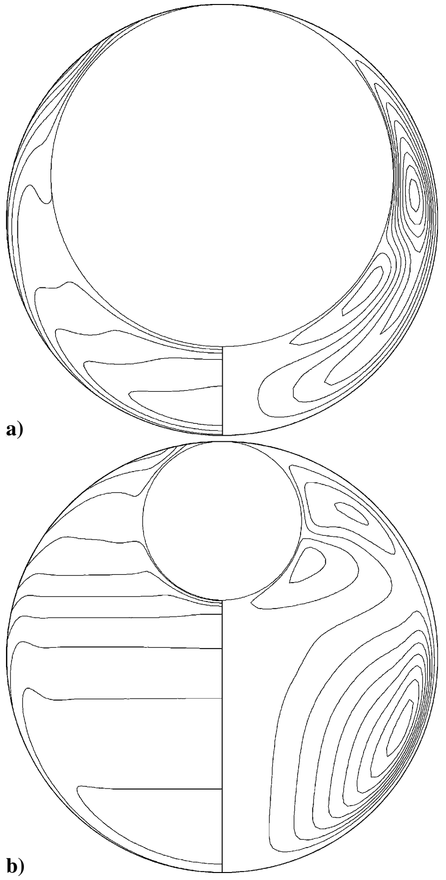

**Fig. 13 Final isotherms and streamlines at $t = 75$ days for a) 50% and b) 95% full tank in microgravity with the spherical vapor region fixed near the wall; minimum and maximum temperatures are a) 23.071 and 23.271 K and b) 21.848 and 22.267 K.**

The final maximum superheat and subcooling are now, respectively, 0.110 and 0.0899 K in Fig. 13a and 0.137 and 0.282 K in Fig. 13b. The maximum superheat is less than it was for the corresponding zero-gravity case, more so for the 95% full tank because there is additional mixing due to natural convection. The maximum flow speed due to natural convection is 0.00401 cm/s in Fig. 13a and 0.00313 cm/s in Fig. 13b. Even though these flows are very weak, they have a definite accumulative effect over the long periods of time considered here. The history of the maximum superheat and subcooling is also shown in Figs. 7 and 8.

The pressure and temperature rise for the flat-interface configuration are shown in Figs. 14 and 15 for both the 50 and 95% fill levels. These curves exhibit the most drastic departure from both the thermodynamic predictions and from the zero-gravity curves in Figs. 2 and 3. This is due to the vapor being in direct contact with the wall and, consequently, receiving much more heat than it needs according to thermodynamics. However, the extra heat cannot leave the vapor region until the conduction boundary layer fully develops on the liquid side of the interface, and that is a relatively slow

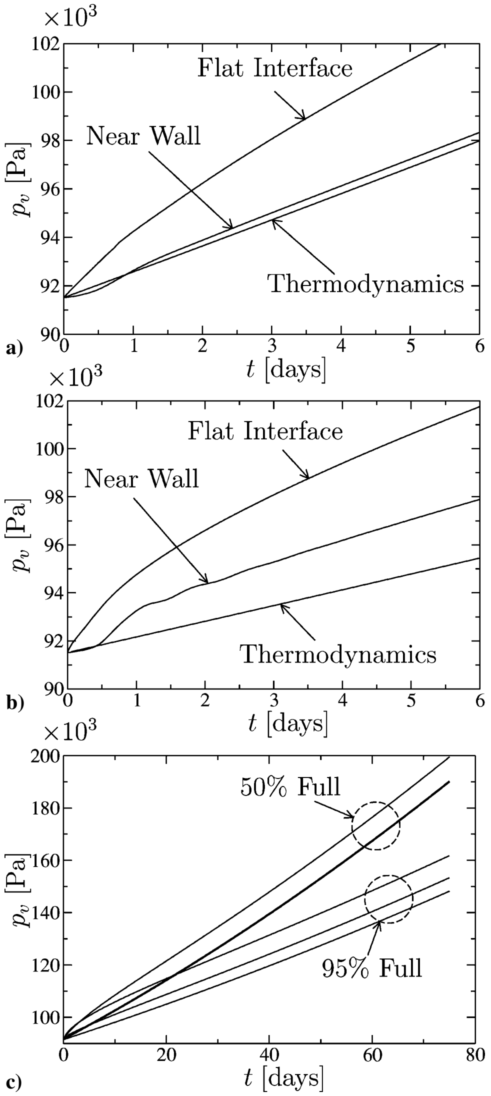

**Fig. 14 Pressure rise for a) 50% and b) 95% full tank in microgravity with two liquid–vapor configurations, namely, a spherical vapor region fixed near the wall and a flat liquid–vapor interface, and c) long-term results for both fill levels.**

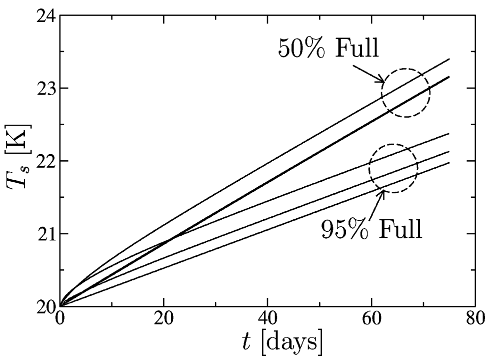

**Fig. 15 Long-term saturation temperatures corresponding to the vapor pressures shown in Fig. 14.**

process. In the meantime, this extra heat goes into raising the vapor pressure at the most rapid rate yet. In all of the preceding cases, heat had to pass through some liquid first before getting into the vapor region, but not in this case. Eventually, the rate of pressure rise agrees with thermodynamics as the net heat flow into the vapor approaches that predicted by thermodynamics.

The final maximum superheat and subcooling are 0.00340 and 0.466 K in Fig. 17a and 0.0000381 and 0.563 K in Fig. 17b. The

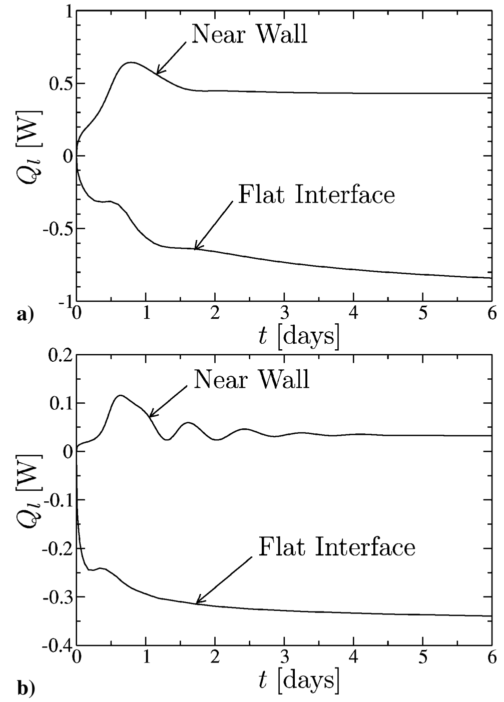

**Fig. 16 Net heat flow into the vapor region through the free surface for the a) 50% and b) 95% full tank in microgravity corresponding to the cases shown in Fig. 14.**

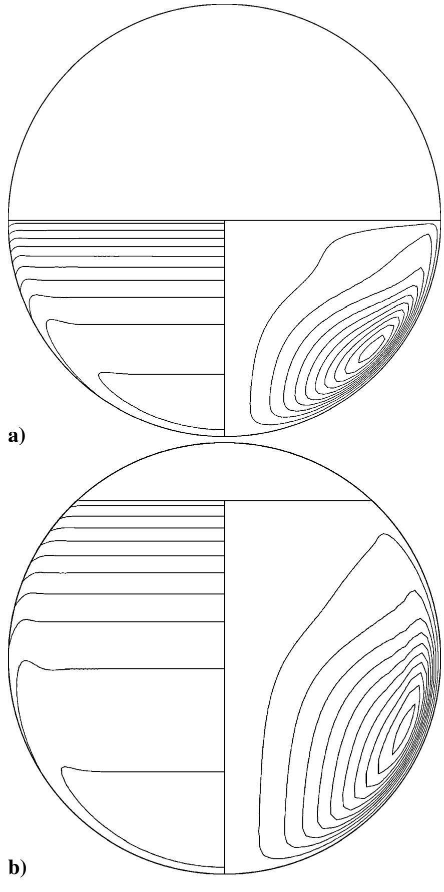

**Fig. 17 Final isotherms and streamlines at $t = 75$ days for a) 50% and b) 95% full tank in microgravity with a flat liquid–vapor interface; minimum and maximum temperatures are a) 22.935 and 23.404 K and b) 21.814 and 22.377 K.**

superheat is so small because the net direction of heat flow across the interface is now reversed (from vapor to liquid) as indicated by the final negative values of $Q_l$ in Fig. 16. The subcooling is very large for that same reason. This actually stabilizes the liquid and reduces the probability of any additional vapor-bubble nucleation. The history of the maximum superheat and subcooling is also shown in Figs. 7 and 8. The maximum flow speed in the liquid is 0.00196 cm/s in Fig. 17a and 0.00278 cm/s in Fig. 17b.

Generally speaking, from these final results, one may also surmise that the configuration of liquid and vapor that minimizes the probability of nucleate boiling would be one in which the vapor completely surrounds a spherical liquid region in the center of the tank. If no liquid is in direct contact with the tank walls, then all of the heat entering the liquid region must go through the vapor first, and this would naturally lead to a situation where the entire liquid region is completely subcooled. Nucleation is not possible in a completely subcooled liquid. This configuration could potentially be achieved by the use of some form of magnetic reorientation, but that idea is left for future work.

## Conclusions

In this paper, we have carefully examined the pressurization of large liquid hydrogen storage tanks by comparing the results from microgravity, zero-gravity, and ground-based numerical case studies. This was done for a number of different liquid–vapor configurations and fill levels. The results show that buoyancy and natural convection are still important in microgravity and cannot be ignored when the pressurization of large cryogenic tanks in space are predicted.

The initial and long-term pressurization rates were determined for several different liquid–vapor configurations and gravity levels. For a large tank in microgravity, the vapor region moves toward the tank wall very quickly when compared to the conduction and natural convection timescales. Thus, long-term pressurization studies were conducted with the vapor region fixed near the wall. For each case, the final rate of pressure rise agrees with the rate predicted by a simpler thermodynamic model, even though the initial pressurization rates depend on the configuration and gravity level. Because of these initial transients, the final pressure levels are also different. In zero gravity, the final pressures are all less than thermodynamic predictions, but, in microgravity, they are all greater than thermodynamics. The initial pressure rise is greatest for the flat-interface configuration because the vapor is in direct contact with the tank wall. In general, the initial rate of pressurization will be greater when more vapor is in direct contact with the wall because it initially receives more heat than is apportioned to it by thermodynamic predictions.

It was also shown that the final rate of pressure rise for a 50% full tank is greater than that for a 95% full tank, regardless of the liquid–vapor configuration. This is not entirely surprising because the simpler thermodynamic model predicts the same result. In general, the rate of pressure rise is less for higher fill levels because a larger fraction of the total heat input goes into raising the liquid temperature, and less heat is available to raise the temperature and pressure of the vapor region.

For relatively large tanks in microgravity, natural convection and buoyancy effects are still important. The results presented here demonstrate this because the pressure rise and thermal stratification are different from those obtained in a zero-gravity environment. The degree of liquid superheat is also lessened due to the mixing effects of natural convection. This is important to know because, as the liquid superheat increases, so does the probability of nucleate boiling, and this can lead to undesirable pressure spikes due to rapid boiling.

It was also shown that the superheat is highest when the vapor region is in the middle of the tank and lowest when more vapor is in direct contact with the tank wall because the net direction of interfacial heat flow is then usually reversed. The best configuration for minimization of the superheat would be to have the liquid region in the middle of the tank completely surrounded by vapor. However, this configuration may not be so desirable because it would also lead to the most rapid changes in pressure due to any changes in the tank wall heat flux. This also implies that the most rapid cooling is achieved if the cryocooler is placed within the vapor region, which would be easier to do if the vapor were touching the wall.

## Acknowledgments

This work was supported by the NASA Office of Biological and Physical Research through the Microgravity Division at NASA Glenn Research Center at Lewis Field. Additional resources were provided by the Computational Microgravity Laboratory and the Microgravity Fluids Physics Branch at NASA John H. Glenn Research Center at Lewis Field.

## References

[1] Salerno, L. J., and Kittel, P., "Cryogenics and the Human Exploration of Mars," *Cryogenics*, Vol. 39, No. 4, 1999, pp. 381–388.

[2] Kittel, P., and Plachta, D. W., "Propellant Preservation for Mars Missions," *Advances in Cryogenic Engineering*, Vol. 45, Plenum, New York, 2000, pp. 443–450.

[3] Panzarella, C. H., and Kassemi, M., "On the Validity of Purely Thermodynamic Descriptions of Two-Phase Cryogenic Fluid Storage," *Journal of Fluid Mechanics*, Vol. 484, June 2003, pp. 136–148.

[4] Aydelott, J. C., "Effect of Gravity on Self-Pressurization of Spherical Liquid-Hydrogen Tankage," NASA TN-D-4286, Dec. 1967.

[5] Aydelott, J. C., "Axial Jet Mixing of Ethanol in Cylindrical Containers During Weightlessness," NASA TP-1487, July 1979.

[6] Aydelott, J. C., "Modeling of Space Vehicle Propellant Mixing," NASA TP-2107, Jan. 1983.

[7] Lin, C. S., Hasan, M. M., and Van Dresar, N. T., "Experimental Investigation of Jet-Induced Mixing of a Large Liquid Hydrogen Storage Tank," AIAA Paper 94-2079, July 1994.

[8] Poth, L. J., and Van Hook, J. R., "Control of the Thermodynamic State of Space-Stored Cryogens by Jet Mixing," *Journal of Spacecraft*, Vol. 9, No. 5, 1972, pp. 332–336.

[9] Lin, C. S., and Hasan, M. M., "Self Pressurization of a Spherical Liquid Hydrogen Storage Tank in a Microgravity Environment," AIAA Paper 92-0363, Jan. 1992.

[10] Vaughan, D. A., and Schmidt, G. R., "Analytical Modeling of No-Vent Fill Process," *Journal of Spacecraft*, Vol. 28, No. 5, 1991, pp. 574–579.

[11] Cha, Y. S., Neiman, R. C., and Hull, J. R., "Thermodynamic Analysis of Helium Boil-off Experiments with Pressure Variations," *Cryogenics*, Vol. 33, No. 7, 1993, pp. 675–679.

[12] Grayson, G. D., Watts, D. A., and Jurns, J. M., "Thermo-Fluid-Dynamic Modeling of a Contained Liquid in Variable Heating and Acceleration Environments," American Society of Mechanical Engineers, ASME Paper FEDSM97-3567, June 1997.

[13] Lin, C. S., and Hasan, M. M., "Numerical Investigation of the Thermal Stratification in Cryogenic Tanks Subjected to Wall Heat Flux," AIAA Paper 90-2375, July 1990.

[14] Navickas, J., "Prediction of a Liquid Tank Thermal Stratification by a Finite Difference Computing Method," AIAA Paper 88-2917, July 1988.

[15] Grayson, G. D., and Navickas, J., "Interaction Between Fluid Dynamic and Thermodynamic Phenomena in a Cryogenic Upper Stage," AIAA Paper 93-2753, Jan. 1993.

[16] Lin, C. S., and Hasan, M. M., "Vapor Condensation on Liquid Surface Due to Laminar Jet-Induced Mixing: The Effects of System Parameters," AIAA Paper 90-0354, Jan. 1990.

[17] Hochstein, J. I., Gerhart, P. M., and Aydelott, J. C., "Computational Modeling of Jet Induced Mixing of Cryogenic Propellants in Low-*g*," AIAA Paper 84-1344, June 1984.

[18] Liu, C. H., "A Numerical Calculation of Time Dependant Dynamical Behavior of Liquid Propellants in a Microgravity Environment," *Microgravity Science and Technology*, Vol. 7, No. 2, 1994, pp. 169–172.

[19] Hung, R. J., and Shyu, K. L., "Constant Reverse Thrust Activated Reorientation of Liquid Hydrogen with Geyser Initiation," *Journal of Spacecraft and Rockets*, Vol. 29, No. 2, 1992, pp. 279–285.

[20] Kothe, D. B., Mjolsness, C. R., and Torrey, M. D., "RIPPLE: A Computer Program for Incompressible Flows with Free Surfaces," Los Alamos National Lab., Rept. LA-12007-MS, Los Alamos, NM, April 1991.

[21] Thornton, R. J., and Hochstein, J. I., "Microgravity Propellant Tank Geyser Analysis and Prediction," AIAA Paper 2001-1132, Jan. 2001.

[22] Marchetta, J. G., and Hochstein, J. I., "Simulation and Dimensionless Modeling of Magnetically Induced Reorientation," AIAA Paper 2000-0700, Jan. 2000.

[23] Marchetta, J. G., Hochstein, J. I., and Sauter, D. R., "Simulation and Prediction of Magnetic Cryogenic Propellant Positioning in Reduced Gravity," AIAA Paper 2001-0930, Jan. 2001.

[24] Peterson, L. D., Crawley, E. F., and Hansman, R. J., "Nonlinear Fluid Slosh Coupled to the Dynamics of a Spacecraft," *AIAA Journal*, Vol. 27, No. 9, 1989, pp. 1230–1240.

[25] Hung, R. J., and Lee, C. C., "Effect of a Baffle on Slosh Waves Excited by Gravity-Gradient Acceleration in Microgravity," *Journal of Spacecraft and Rockets*, Vol. 31, No. 6, 1994, pp. 1107–1114.

[26] Reif, F.," *Fundamentals of Statistical and Thermal Physics*, McGraw–Hill, New York, 1965, p. 306.

[27] Engelman, M. S., and Sani, R. L., "Finite Element Simulation of Incompressible Fluid Flows with a Free/Moving Surface," *Computational Techniques for Fluid Flow*, Pineridge, Swansea, Wales, U.K., 1986, pp. 47–74.

[28] Gresho, P. M., Lee, R. L., and Sani, R. C., "On the Time-Dependent Solution of the Incompressible Navier–Stokes Equations in Two and Three Dimensions," *Recent Advances in Numerical Methods in Fluids*, Vol. 1, Pineridge, Swansea, Wales, U.K., 1979, pp. 27–79.

[29] Panton, R., *Incompressible Flow*, Wiley, New York, 1984, p. 557.

W. Williamson
*Associate Editor*